AEROSOL OPTICS

Amplification of light within aerosol particles accelerates in-particle photochemistry

Pablo Corral Arroyo[1], Grégory David[1], Peter A. Alpert[2], Evelyne A. Parmentier[1], Markus Ammann[2], Ruth Signorell[1]*

Optical confinement (OC) structures the optical field and amplifies light intensity inside atmospheric aerosol particles, with major consequences for sunlight-driven aerosol chemistry. Although theorized, the OC-induced spatial structuring has so far defied experimental observation. Here, x-ray spectromicroscopic imaging complemented by modeling provides direct evidence for OC-induced patterning inside photoactive particles. Single iron(III)–citrate particles were probed using the iron oxidation state as a photochemical marker. Based on these results, we predict an overall acceleration of photochemical reactions by a factor of two to three for most classes of atmospheric aerosol particles. Rotation of free aerosol particles and intraparticle molecular transport generally accelerate the photochemistry. Given the prevalence of OC effects, their influence on aerosol particle photochemistry should be considered by atmospheric models.

Atmospheric aerosol particles are suspensions of solid and liquid particles in air that influence both climate and air quality (*1*). Aerosol and cloud chemistry play a crucial role in the processing of atmospheric particulate matter and are key parts of global atmospheric models (*2*–*6*). Chemical reactions triggered by sunlight in the gas and particle phase have been recognized as a major contributor to the degradation and oxidation of matter in atmospheric aerosols (*7*). Energy- or charge-transfer reactions driven by triplet states (*8*–*10*), photolysis of nitrate and nitrite (*11*), and photolysis of iron carboxylate complexes (*12*, *13*) are examples of atmospherically relevant photochemical processes that involve the particle phase. Photochemical reactions can also be promoted at the surface of atmospheric aerosol particles (*14*–*16*). It has been reported that interface effects and surface charging can cause acceleration of chemical reactions in microdroplets and nanodroplets (*14*, *17*–*20*), observations that have especially sparked interest in the use of microdroplets as new powerful reactors for chemical synthesis (*15*, *16*).

Here, we report another intriguing phenomenon in particle reactions: the influence of optical confinement (OC) on photochemical reactions in aerosol particles (*21*). OC leads to spatial structuring of the light intensity inside the particle [nanofocusing or shadowing; see supplementary materials (SM) section S1] (*21*–*24*) and hence to spatial variations of photochemical rates. For a photochemical reaction step, the overall reaction rate, *j*, in a particle is given by

$$j = \frac{I(\lambda)\lambda}{hc}\varphi(\lambda)\sigma(\lambda)\int\varepsilon\left(n,k,\vec{r},\lambda\right)C\left(\vec{r}\right)\mathrm{d}\vec{r} \qquad (1)$$

where $\vec{r}$ is the position in the particle; the local light-enhancement factor, $\varepsilon\left(n,k,\vec{r},\lambda\right)$, is the ratio of the local light intensity, $I_{\mathrm{p}}\left(\vec{r}\right)$, to the incident light intensity, I; λ is the wavelength of the light; h is Planck's constant; c is the speed of light; n and k are the real and imaginary parts of the complex index of refraction, respectively; φ is the quantum yield; σ is the molecular absorption cross section; and $C\left(\vec{r}\right)$ is the molecular density of the reactant. Shadowing results from strong light absorption (high k values), reducing the average light intensity in the particle. Because shadowing is also present in extended condensed systems (referred to as "bulk"), particle and bulk reaction rates are comparable in this case (*21*). Nanofocusing is a resonance phenomenon that is tied to the spatial confinement by particles. It increases the average light intensity in the particle compared with the incident intensity—that is, on average, $\varepsilon > 1$—thereby accelerating the reaction (Eq. 1) in particles compared with that in bulk systems, where nanofocusing does not occur. The influence of ε on photokinetics and radiation balance can be substantial, but atmospheric models do not usually account for it. The acceleration of photochemical reactions in typical atmospheric aerosol particles is still awaiting a comprehensive evaluation. Although basic research has demonstrated the overall acceleration of photochemical reactions in single aerosol droplets (*21*), the predicted spatial variation of photochemical rates induced by OC effects has not been directly observed or quantitatively constrained within submicron aerosol particles until now.

Here, we directly imaged the local compositional gradients resulting from OC inside single submicrometer-sized particles (Fig. 1). Highly viscous, dried Fe(III)–citrate (FeCit) particles were exposed to ultraviolet (UV) light ($h\nu$, where ν is the photon frequency), resulting in the photoreduction to Fe(II):

$$\mathrm{Fe^{III}Cit} \xrightarrow{h\nu} \mathrm{Fe^{II}}\left(\mathrm{Cit}^{\bullet}\right) \qquad (2)$$

Scanning transmission x-ray microscopy coupled with near-edge x-ray absorption fine structure (STXM-NEXAFS) spectroscopy was used to image the temporal evolution of the Fe (III) fraction, α (eq. S2). A quantitative model proves that OC effects are responsible for the

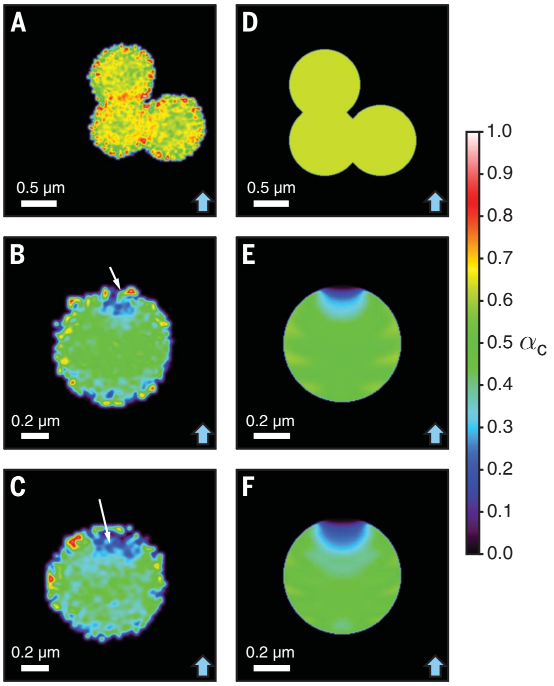

Fig. 1. Maps of the Fe(III) fraction upon UV photoreduction of iron in submicron FeCit particles. (**A** to **F**) STXM-NEXAFS experiments [(A) to (C)] and simulations [(D) to (F)] of the column-averaged Fe(III) fraction, α_c (see color scale bar). α_c is shown before irradiation [(A) and (D)] and after 94 min [(B) and (E)] and 139 min [(C) and (F)] of irradiation with UV light in the direction indicated by the blue arrow. α_c is averaged along the x-ray–beam propagation direction, which is perpendicular to the UV-light propagation direction (fig. S2). The white arrows indicate the hotspot region that is due to nanofocusing.

---

[1] Department of Chemistry and Applied Biosciences, ETH Zürich, Vladimir-Prelog-Weg 2, CH-8093 Zürich, Switzerland.
[2] Laboratory of Environmental Chemistry, Paul Scherrer Institute, 5232 Villigen PSI, Switzerland.
***Corresponding author. Email: rsignorell@ethz.ch**

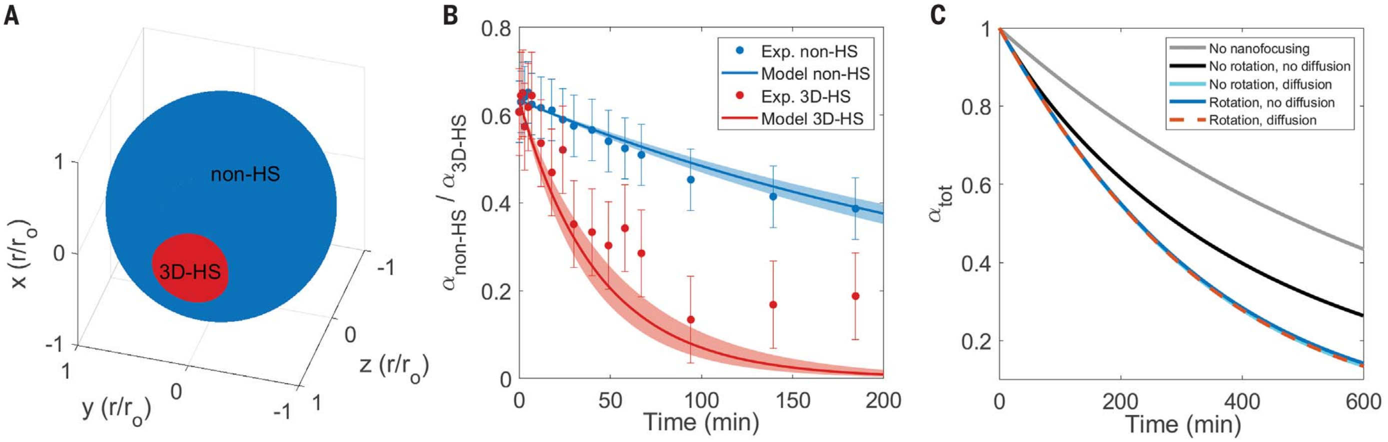

Fig. 2. Influence of nanofocusing, diffusion, and particle rotation on the UV photoreduction of Fe(III) in submicron FeCit particles. (**A**) 3D representation of a particle showing the 3D-hotspot region (red) and the non-hotspot region (blue) (SM section S5). (**B**) Fe(III) fraction in the hotspot region ($\alpha_{3D\text{-}HS}$) and the non-hotspot ($\alpha_{non\text{-}HS}$) region. Circles and curves show experimental data from STXM measurements (SM section S5) and simulations (SM section S7), respectively. The initial Fe(III) ratio was $\alpha(t = 0) = 0.634$. The experimental error bars are either ±0.07 (*28*) or the standard deviations of propagated photon counts, whichever is larger. The shaded regions represent the uncertainty of the model prediction that arises from the experimental uncertainty of the decay rate coefficient in the non-hotspot region ($\beta_{non\text{-}HS}$; SM section S5) and from the uncertainty in the real part of the refractive index (1.5 ± 0.05). (**C**) Photochemical decay of the Fe(III) fraction averaged over the whole particle, $\alpha_{tot}(t)$, calculated for initial iron fractions $\alpha(t = 0) = 1$ and particle radii of 320 nm for five different cases: a particle without rotation and diffusion as in (B) (black trace; SM section S7); a particle without rotation, diffusion, or nanofocusing (gray trace; SM section S8); a particle without rotation but with diffusion (light blue trace; SM section S11); a particle with rotation but no diffusion (dark blue trace; SM section S9); and a particle with rotation and diffusion (dashed orange trace; SM sections S9 and S11).

overall acceleration of the reaction and the spatial inhomogeneity of α that was observed experimentally. Based on this result, we predict how OC effects enhance photochemical reactions in a range of typical atmospheric aerosol particles that are exposed to solar radiation, demonstrating the importance of the phenomenon for the fate of aerosols in the atmosphere.

Figure 1, A to C, shows representative STXM-NEXAFS images of the column-averaged Fe(III) fraction, α_c (see fig. S2A), of FeCit particles acquired before UV irradiation and after 94 and 139 min of UV irradiation ($\lambda \sim 367$ nm), respectively (SM sections S2 to S5). The inhomogeneous spatial depletion of Fe(III) inside the particle that arises from OC effects is clearly visible opposite the side of incidence of the UV light (blue arrow). The white arrows indicate the "hotspot" (Fig. 2A), where the photoreduction is faster than elsewhere in the particle (Fig. 2B). This pattern is the result of nanofocusing, which increases the local light intensity in the hotspot, as confirmed by images simulated for particles with a radius, r_0, of 320 nm (Fig. 1, D to F). The simulations were based on a three-dimensional (3D) particle model that combines light-intensity calculations using the discrete dipole approximation [(*25*) and SM section S6] with a photochemical model for the decay of Fe(III) (SM sections S4 and S7). The results in Fig. 1 are direct observations of the spatial patterning of photochemical reaction products by nanofocusing.

Spatial inhomogeneity was quantified by evaluating the decay of α in two regions within the particle (Fig. 2A and SM section S5): in the 3D hotspot ($\alpha_{3D\text{-}HS}$), where the light intensity was strongly amplified, and in the rest of the particle, which is referred to as the non-hotspot region ($\alpha_{non\text{-}HS}$). The substantially faster decay of $\alpha_{3D\text{-}HS}$ compared with that of $\alpha_{non\text{-}HS}$ (Fig. 2B) highlights the pronounced spatial inhomogeneity of the photoreduction rates caused by OC effects within submicron particles, which is in good agreement with the simulated photochemical decay curves in Fig. 2B (SM section S7). Nanofocusing not only makes the photolysis spatially inhomogeneous but also results in an overall acceleration compared with the reaction in bulk. This becomes evident in the decay of the Fe(III) averaged over the whole particle, α_{tot}, as illustrated in Fig. 2C for simulated decay curves of initially pure FeCit [$\alpha(t = 0) = 1$, where t is the reaction time]. The black decay curve represents the case with nanofocusing, whereas the gray curve corresponds to a hypothetical case without nanofocusing that represents the situation in bulk (SM section S8). In this specific example, the nanofocusing is only moderate but still results in a clear acceleration of the reaction in the particle compared with the reaction in bulk. In other situations, typical of certain atmospheric aerosols, the acceleration is usually even more pronounced (vide infra).

Diffusion time scales of organic molecules within atmospheric secondary organic aerosol (SOA) particles, τ_{mix} (*26*), are compared with a typical photochemical time scale of τ_{photo} = 1 hour in fig. S7. A wide range of diffusivities are included, with an increasing abundance of viscous particles (*27*) (hence with low diffusivity) at higher altitudes. The FeCit particles discussed so far were highly viscous such that diffusion was negligible. For less-viscous atmospheric aerosol particles, however, diffusion needs to be accounted for. To illustrate its effect, Fig. 2C shows the photodecay of a hypothetical FeCit particle with instantaneous diffusion (light blue trace). The comparison with the highly viscous case (black trace) shows that diffusion can further accelerate photochemical reactions when OC effects are present. Diffusion constantly replenishes regions of enhanced light intensity (hotspot) with fresh reactant.

A similar acceleration can result from the free rotation of atmospheric particles, when τ_{photo} is longer than the time scale of rotation. Typical rotation time scales of atmospheric particles in air are shorter than a few hundred milliseconds, whereas atmospheric aerosol photochemistry commonly occurs on time scales, $\tau_{photo,}$ from seconds to hours (*7*, *10*, *12*, *13*). Over time, fast particle rotation leads to a better overlap between regions of high reactant concentration and regions of enhanced light intensity (hotspot). Thus, fast rotation amounts to angularly averaging the OC effects. We describe this in terms of a radial light-enhancement factor, ε_r, and a radial Fe(III)

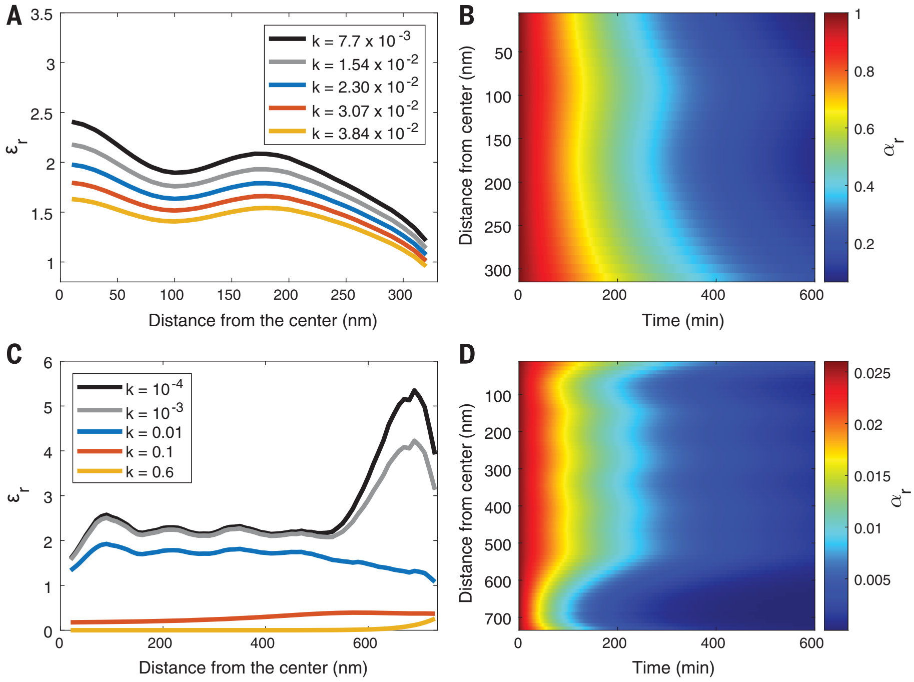

Fig. 3. Radial dependence of light enhancement and Fe(III) fraction in the photoreduction of Fe(III) in rotating FeCit particles. All simulations are for highly viscous (no diffusion), fast-rotating particles for λ = 367.7 nm light, n = 1.5, and φ = 0.016 ± 0.003. (**A** and **B**) Calculations for a fast-rotating particle with radius r_0 = 320 nm and k values that represent experimental conditions (Figs. 1 and 2). Shown in (A) is the radial enhancement factor, ε_r, for selected k values that correspond to experimental Fe(III) fractions of 0.2, 0.4, 0.6, 0.8, and 1, respectively, as a function of the distance from the particle center (0 nm). Shown in (B) are the radial Fe(III) fractions, $\alpha_r(t)$, as a function of the distance from the particle center and the reaction time for $\alpha_r(t = 0) = 1$. ε_r and α_r are obtained by averaging over polar and azimuthal angles (SM section S9). (**C**) Calculations of ε_r for a fast-rotating particle with radius r_0 = 735.4 nm and k values between 10^{-4} (weakly absorbing particle) and 0.6 (strongly absorbing particle). (**D**) Decay of α_r in a rotating particle with radius r_0 = 735.4 nm as a function of time for $\alpha_r(t = 0) = 0.026$.

fraction, $\alpha_r(t)$ (SM section S9). Figure 3A shows ε_r as a function of the distance from the particle center calculated for homogeneous FeCit particles with different Fe(III) concentrations given by the corresponding value of the complex indices of refraction, k. Because the hotspot makes up only a small part of the volume of the particle's outermost layer, angular averaging actually causes ε_r to be smaller near the particle's surface than in its interior. This behavior of ε_r is reflected in the temporal evolution of the radial Fe(III) fraction, $\alpha_r(t)$, in Fig. 3B. α_r decays faster in the interior of the particle than close to its surface, which indicates the persistence of concentration gradients produced by OC effects in viscous particles, in a similar way as observed for the slow reactive uptake of oxygen (*28*). Nevertheless, the decay of Fe(III) averaged over the entire particle, α_{tot} (dark blue trace in Fig. 2C), is still faster than that in the nonrotating particle (black trace). Rotation (dark blue trace) and diffusion (light blue trace) each accelerate the photoreduction to virtually the same extent once they are much faster than the photochemical time scale, as evident from the coincidence of the corresponding traces. In these cases, the acceleration reaches an upper limit that is not surpassed even by simultaneous rotation and diffusion (dashed orange trace). This has an important implication for atmospheric aerosol particles: Because the time scale for particle rotation is typically faster than τ_{photo}, it invariably leads to an acceleration of the photochemistry even if diffusion is slow. Whenever the initial reactant distribution is sufficiently homogeneous, the maximum acceleration is almost reached by rotation alone. Further acceleration by fast diffusion occurs to a limited extent in larger, weakly light-absorbing particles (Fig. 3, C and D).

In cases of a pronounced optical resonance—for example, the excitation of whispering gallery modes (*24*)—the light enhancement near the surface is no longer limited to a single hotspot but instead extends over a large part of the surface layer. Such strong resonances are commonly found in larger particles, as exemplified by a 735-nm particle in Fig. 3, C and D. In contrast to the case of the 320-nm particle (Fig. 3A), the strong enhancement of the light intensity in the surface layer survives the rotational averaging. The result is the pronounced peak in the black and gray traces of ε_r in Fig. 3C. This is again reflected in the temporal evolution of $\alpha_r(t)$ in Fig. 3D: Contrary to the behavior of the smaller particle (Fig. 3B), α_r now decays faster close to the surface of the particle than in the particle's interior. This illustrates the rich variability of the spatial structuring of photochemistry in aerosol particles that is induced by optical resonance effects.

When the light absorption in the particle increases (i.e., increasing k values in Fig. 3C), the light enhancement becomes weaker until the peak near the particle's surface vanishes altogether (blue curve), and ε_r finally drops below one throughout the particle (orange and yellow curves). This is the situation when shadowing dominates (fig. S1B). In this case, there is no acceleration of the photochemistry in particles compared with bulk reactions, which are similarly affected by shadowing (*21*). Such strongly absorbing particles, however, tend to be rare in the atmosphere (see below). We conclude that the resonance effects discussed above generally dominate and accelerate photochemical reactions in particles compared with their bulk counterparts.

With the above results, we assess the influence of OC effects on photochemical reactions in atmospheric aerosol particles. In Fig. 4, we predict the total light-enhancement factor, ε_{tot} (eq. S15), for a range of aerosol particles and conditions relevant to Earth's atmosphere (particle size, refractive index, solar radiation; SM sections S12 and S13). Figure 4A shows the dependence of ε_{tot} on light absorptivity (in terms of k) and particle size (r_0) as the most important parameters. Without loss of generality, we assume spherical particles with a constant n = 1.5. The dashed colored rectangles indicate the typical ranges of absorptivity and particle size for various classes of atmospheric particles, that is, SOA particles (black) (*29*, *30*), humic-like substances (HULIS) particles (blue) (*31*), urban particles (red), rural particles (green) (*32*), soot (brown) (*33*), organic biomass burning particles (purple) (*34*), and sea salt particles (white) (*35*). Calculations for specific substances, accounting for the wavelength dependence of the refractive index, are shown in Fig. 4B for water (*36*); SOA material from limonene, from α-pinene, and from catechol (*29*); and brown carbon (BrC) (*37*). ε_{tot} values less than one (shadowing)—as observed for highly absorbing larger BrC particles—are very rare for atmospheric particles.

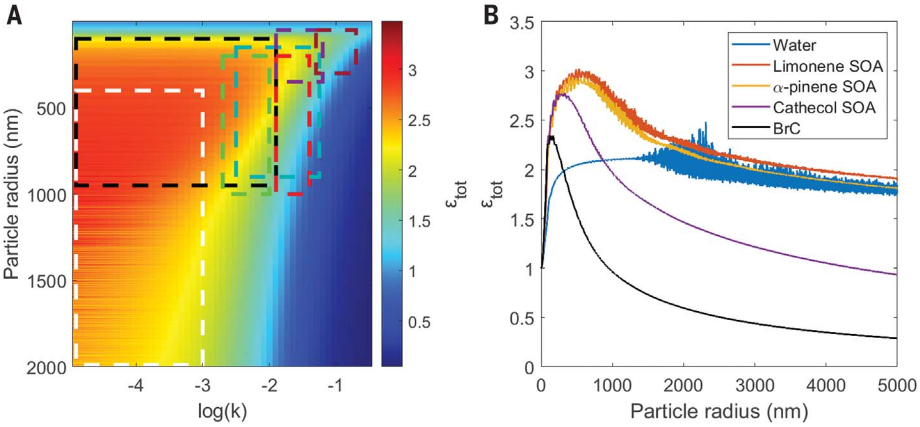

Fig. 4. OC effects in typical atmospheric aerosol particles. (**A**) The total light-enhancement factor, ε_{tot} (see color scale bar), for spherical particles averaged over the wavelength range of 280 to 440 nm as a function of the particle radius (r_0) and the imaginary part of the refractive index (k) for constant n = 1.5 (SM section S12). The dashed colored rectangles indicate the range of properties for different classes of ambient aerosol particles: SOA particles (black), HULIS particles (blue), urban particles (red), rural particles (green), soot (brown), organic biomass burning particles (purple), and sea salt particles (white). (**B**) ε_{tot} as a function of the particle radius for SOA material from limonene, α-pinene, and catechol and for BrC particles. These predictions are for spherical particles using wavelength-dependent refractive index data for the respective materials from the literature in the wavelength range of 280 to 440 nm. For the averaging over the wavelength range of 280 to 440 nm, the relative contribution of each wavelength was weighted according to its relative intensities in sunlight (SM section S12).

Figure 4 shows that enhancement factors for most other atmospheric aerosols lie between two and three, typically reaching their maximum for PM2.5 particles (r_0 < 1.25 μm). The results for water (blue trace in Fig. 4B) show that light-enhancement factors around two are also expected in cloud droplets, certainly up to sizes of many micrometers. Accounting for ε_{tot} in clouds could improve predictions of radical formation in clouds (*38*) and of the formation of aqueous SOAs (*39*).

With typical light-enhancement factors of two to three attained by most atmospheric particles, photochemical reactions in these particles are generally expected to be accelerated on average by the same factor. Accounting for ε_{tot} in SOAs should improve the prediction of the SOA evolution (*40*). This might explain the mismatch between observations and model predictions of SOA mass loss by a factor of two to three, as reported by Hodzic *et al.* (*41*). They used a chemical model to simulate the evolution of submicron α-pinene SOA particles under aging conditions and applied their results to a global chemistry model; however, OC effects were not considered. Given that the authors found photolysis in the particle phase to be a dominant degradation pathway of SOAs, it appears plausible that the neglect of the acceleration of photochemical reactions by light-enhancement effects in the aerosol particles could contribute to the reported discrepancy between model and observation.

Our study provides evidence that light-enhancement effects in typical aerosol particles are more important for photochemical reactions than previously anticipated. For most atmospheric aerosol particles, we argue that an acceleration of photochemical reactions compared with bulk reactions will occur. In view of its prevalence, atmospheric aerosol and cloud models should now account for this phenomenon to improve global chemistry models and climate predictions.

REFERENCES AND NOTES

1. U. Pöschl, *Angew. Chem. Int. Ed.* **44**, 7520–7540 (2005).
2. J. L. Jimenez *et al.*, *Science* **326**, 1525–1529 (2009).
3. M. E. Monge *et al.*, *Proc. Natl. Acad. Sci. U.S.A.* **109**, 6840–6844 (2012).
4. A. Tilgner, P. Bräuer, R. Wolke, H. Herrmann, *J. Atmos. Chem.* **70**, 221–256 (2013).
5. M. Shiraiwa *et al.*, *Proc. Natl. Acad. Sci. U.S.A.* **110**, 11746–11750 (2013).
6. A. Laskin *et al.*, *Science* **301**, 340–344 (2003).
7. C. George, M. Ammann, B. D'Anna, D. J. Donaldson, S. A. Nizkorodov, *Chem. Rev.* **115**, 4218–4258 (2015).
8. S. Canonica, *Chimia* **61**, 641–644 (2007).
9. K. McNeill, S. Canonica, *Environ. Sci. Process. Impacts* **18**, 1381–1399 (2016).
10. P. Corral Arroyo *et al.*, *Environ. Sci. Technol.* **52**, 7680–7688 (2018).
11. H. Herrmann *et al.*, *J. Atmos. Chem.* **36**, 231–284 (2000).
12. C. Weller, A. Tilgner, P. Bräuer, H. Herrmann, *Environ. Sci. Technol.* **48**, 5652–5659 (2014).
13. J. Dou *et al.*, *Atmos. Chem. Phys.* **21**, 315–338 (2021).
14. J. M. Anglada, M. T. C. Martins-Costa, J. S. Francisco, M. F. Ruiz-López, *J. Am. Chem. Soc.* **142**, 16140–16155 (2020).
15. K. J. Kappes *et al.*, *J. Phys. Chem. A* **125**, 1036–1049 (2021).
16. S. Banerjee, E. Gnanamani, X. Yan, R. N. Zare, *Analyst* **142**, 1399–1402 (2017).
17. R. M. Bain, C. J. Pulliam, R. G. Cooks, *Chem. Sci.* **6**, 397–401 (2015).
18. T. Müller, A. Badu-Tawiah, R. G. Cooks, *Angew. Chem. Int. Ed.* **51**, 11832–11835 (2012).
19. P. Nissenson, C. J. H. Knox, B. J. Finlayson-Pitts, L. F. Phillips, D. Dabdub, *Phys. Chem. Chem. Phys.* **8**, 4700–4710 (2006).
20. D. L. Bones, L. F. Phillips, *Phys. Chem. Chem. Phys.* **11**, 5392–5399 (2009).
21. J. W. Cremer, K. M. Thaler, C. Haisch, R. Signorell, *Nat. Commun.* **7**, 10941 (2016).
22. R. Signorell *et al.*, *Chem. Phys. Lett.* **658**, 1–6 (2016).
23. Y. Zhang *et al.*, *NPJ Clim. Atmos. Sci.* **1**, 47 (2018).
24. R. Symes, R. M. Sayer, J. P. Reid, *Phys. Chem. Chem. Phys.* **6**, 474–487 (2004).
25. M. A. Yurkin, A. G. Hoekstra, *J. Quant. Spectrosc. Radiat. Transf.* **112**, 2234–2247 (2011).
26. M. Shiraiwa *et al.*, *Nat. Commun.* **8**, 15002 (2017).
27. A. Virtanen *et al.*, *Nature* **467**, 824–827 (2010).
28. P. A. Alpert *et al.*, *Nat. Commun.* **12**, 1769 (2021).
29. P. Liu, Y. Zhang, S. T. Martin, *Environ. Sci. Technol.* **47**, 13594–13601 (2013).
30. P. F. Liu *et al.*, *Atmos. Chem. Phys.* **15**, 1435–1446 (2015).
31. E. Dinar *et al.*, *Faraday Discuss.* **137**, 279–295 (2008).
32. M. Ebert, S. Weinbruch, P. Hoffmann, H. M. Ortner, *Atmos. Environ.* **38**, 6531–6545 (2004).
33. J. Kim *et al.*, *Aerosol Sci. Technol.* **49**, 340–350 (2015).
34. E. Sarpong, D. Smith, R. Pokhrel, M. N. Fiddler, S. Bililign, *Atmosphere* **11**, 62 (2020).
35. L. Bi *et al.*, *J. Geophys. Res. Atmos.* **123**, 543–558 (2018).
36. G. M. Hale, M. R. Querry, *Appl. Opt.* **12**, 555–563 (1973).
37. J. Li *et al.*, *Atmos. Chem. Phys.* **20**, 4889–4904 (2020).
38. H. Herrmann *et al.*, *Chem. Rev.* **115**, 4259–4334 (2015).
39. B. Ervens, B. J. Turpin, R. J. Weber, *Atmos. Chem. Phys.* **11**, 11069–11102 (2011).
40. M. Shrivastava *et al.*, *Rev. Geophys.* **55**, 509–559 (2017).
41. A. Hodzic *et al.*, *Atmos. Chem. Phys.* **15**, 9253–9269 (2015).
42. P. Corral Arroyo *et al.*, Data Collection: Amplification of light within aerosol particles accelerates in-particle photochemistry. ETH Zürich (2022); https://doi.org/10.3929/ethz-b-000531184.
43. G. David, Registered software: "Particle_internal_intensity_enhancement_factor.py". ETH Zürich (2022); https://doi.org/10.5905/ethz-1007-500.

ACKNOWLEDGMENTS

We acknowledge B. Watts for support during the beamtime at the PolLux end station of the Swiss Light Source and M. Shiraiwa and Y. Li for sharing their global maps of SOA viscosity (fig. S7). **Funding:** This project has received funding from the Swiss National Science Foundation (project 200020_200306) and the European Research Council (Horizon 2020 Research and Innovation Programme grant agreement 786636). The PolLux end station was financed by the German Ministerium für Bildung und Forschung (BMBF) through contracts 05K16WED and 05K19WE2. **Author contributions:** Conceptualization: P.C.A., R.S.; Methodology: P.C.A., G.D., P.A.A., R.S.; Investigation: P.C.A., G.D., P.A.A., E.A.P.; Funding acquisition: R.S.; Project administration: P.C.A., R.S.; Supervision: R.S.; Writing – original draft: P.C.A., G.D., R.S.; Writing – review and editing: P.C.A., G.D., R.S., E.A.P., P.A.A., M.A. **Competing interests:** The authors declare no conflicts of interest. **Data and materials availability:** All data that reproduce the analyses are available in a data repository (*42*). A Python program for the calculations of enhancement factors (SM section S12) is available in a project-associated data archive repository (*43*).

SUPPLEMENTARY MATERIALS

science.org/doi/10.1126/science.abm7915
Supplementary Text
Figs. S1 to S8
References (*44*–*51*)
Movies S1 and S2

12 October 2021; accepted 14 March 2022
10.1126/science.abm7915